J. Fluid Mech. (2000), *vol.* 402, *pp.* 33–56. Printed in the United Kingdom

© 2000 Cambridge University Press

On the competition between centrifugal and shear instability in spiral Couette flow

By A. MESEGUER[1] AND F. MARQUES[2]

[1]Oxford University Computing Laboratory (OUCL), Wolfson Building, Parks Road, Oxford OX1 3QD, UK

[2]Dep. Física Aplicada, Universitat Politècnica de Catalunya, Jordi Girona Salgado s/n, Mòdul B4 Campus Nord, 08034 Barcelona, Spain

(Received 4 May 1998 and in revised form 29 July 1999)

The linear stability of a fluid confined between two coaxial cylinders rotating independently and with axial sliding (spiral Couette flow) is examined. A wide range of experimental parameters has been explored, including two different radius ratios. Zeroth-order discontinuities are found in the critical surface; they are explained as a result of the competition between the centrifugal and shear instability mechanisms, which appears only in the co-rotating case, close to the rigid-body rotation region. In the counter-rotating case, the centrifugal instability is dominant. Due to the competition, the neutral stability curves develop islands of instability, which considerably lower the instability threshold. Specific and robust numerical methods to handle these geometrical complexities are developed. The results are in very good agreement with the experimental data available, and with previous computations.

1. Introduction

We consider an incompressible viscous fluid which is contained in the gap between two concentric cylinders that rotate independently about a common axis at constant angular velocities. Forward motion is induced by an inertial sliding of the cylinders relative to one another along the pipe axis. The basic motion whose linear stability will be studied is, therefore, a combination of the Couette flow and the axial velocity field induced by the relative sliding, the so-called spiral Couette flow (Joseph 1976).

This problem was first studied by Kiessling (1963) and Ludwieg (1964), who obtained inviscid stability criteria in the narrow gap case. The experiments of Ludwieg (1964) are, as far as we know, the only experiments on this problem until now. The results showed the correctedness of the inviscid Ludwieg (1964) criterion (see figure 12), later improved by Wedemeyer (1967). The general problem was studied by Mott & Joseph (1968) and by Hung, Joseph & Munson (1972) with special emphasis on energy methods; an excellent review can be found in the book Joseph (1976, chap. VI). Recently, Ali & Weidman (1993) did a linear stability analysis of spiral Couette flow, in the stationary outer cylinder case, for the so-called enclosed geometry, which includes end effects. The more general problem of oscillatory sliding has been recently considered by Hu & Kelly (1995) and Marques & Lopez (1997), whose numerical simulations are in good agreement with the experiments of Weisberg, Smits & Kevrekidis (1997). All of these works considered the infinite cylinders case, assuming periodicity in the axial direction. As a result of the sliding, a non-zero mean flow in the axial direction appears, which can only exist in open-ended configurations,

like in the experiments of Ludwieg (1964). The presence of lids enforces a zero axial mean flow; this constraint is implemented by adding a suitable axial pressure gradient, which mimics the lid effect, preserving the periodicity of the velocity field; this is the so-called enclosed case.

An understanding of the stability of these flows could have applications in some industrial processes like the purification of industrial waste water (Ollis, Pelizzetti & Serpone 1991), the production of wire and cables (Tadmor & Bird 1974) and optical fibre fabrication techniques (Chida *et al.* 1982). In all of them, axial sliding in a cylindrical annulus takes place, and the rotation of one or both cylinders changes the stability and properties of the flow.

This paper presents an extensive exploration of the linear stability of spiral Couette flow mainly in the open ends case in order to compare with existing experimental data, although some computations are performed for the enclosed configuration in order to test our numerical code and quantify the effect of end caps. The exploration covers a wide range of angular velocities of both cylinders, and two different radius ratios are examined: one corresponds to the Ludwieg (1964) experiment, with a radius ratio $\eta = 0.8$ close to the narrow gap case ($\eta \to 1$). The other case (with a wide gap $\eta = 0.5$) has been considered because the instability appears at lower Reynolds numbers than in the narrow gap case, and the change in the azimuthal wavenumbers to be considered is also smaller, which permits a more detailed analysis.

It has long been known that whenever two or more control parameters representing different physical mechanisms for instability compete, one can observe stability turning points, islands of stability, multiple minima, and large changes in the critical azimuthal wavenumber. Examples include the competition between buoyancy and shear in inclined natural convection (Hart 1971), between buoyancy-induced shear and rotation in radial Couette flow (Ali & Weidman 1990), between centrifugal and Kelvin–Helmholtz instabilities in swirling jets (Martin & Meiburg 1994) and between rotation and axial sliding in modulated Taylor–Couette flow (Marques & Lopez 1997). There are also examples of complicated neutral curve topology in crystal–melt interface problems as studied by McFadden *et al.* (1990). In the present problem the competition between wall-driven shear and centrifugal instability mechanisms is responsible for the geometrical complexities.

The paper is organized as follows. In § 2, a complete description of the physical system is given, and the analytical steady solutions are computed for the general case. In § 3 the linear differential equations which govern the stability of the first-order perturbations are obtained, using a Petrov–Galerkin scheme. The symmetries of the problem are considered in order to reduce the parameter space region to be explored. The neutral stability curves in this problem may have multiple extrema and exhibit sharp geometrical forms with sometimes disconnected parts. Specific and robust methods for obtaining the neutral stability curves with such complex geometries are designed. The results of our numerical method are checked with results obtained previously by Ali & Weidman (1993). Section 4 is concerned with the wide gap case $\eta = 0.5$. For each pair of values of R_o and R_z (outer rotation Reynolds number and axial Reynolds number respectively) the neutral stability surface is computed. Complex behaviour is found in the co-rotation zone, in particular as the axial Reynolds number is increased. In fact, discontinuities in the critical inner rotation Reynolds number surface have been observed. This phenomenon is explained in detail as a competition between the centrifugal instability mechanism characteristic of the Taylor–Couette problem and the shear instability mechanism induced by the axial sliding. This interpretation is reinforced by examining the rigid rotation case with

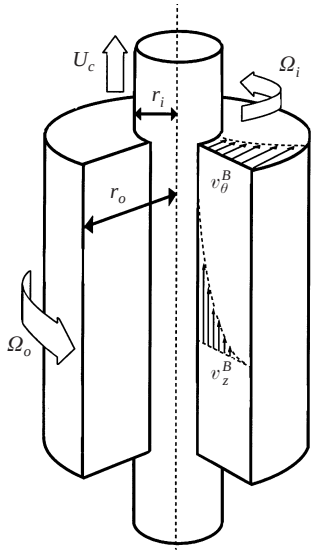

FIGURE 1. Geometric sketch and parameters of the Taylor–Couette problem with axial sliding. The basic flow v_B, w_B, driven by the axial motion U_c and the angular rotations Ω_i, Ω_o, is also depicted.

sliding. Section 5 deals with the narrow gap case $\eta = 0.8$, where the same features are present. The results are compared with the experimental results of Ludwieg (1964) and the linear stability computations of Hung *et al.* (1972), obtaining a very good agreement with both. A detailed analysis of the experimental data shows the presence of hysteresis regions associated with the aforementioned discontinuities. Finally, § 6 draws some conclusions.

2. Steady solutions

Taylor–Couette flow is the term used to describe fluid motion between two concentric rotating cylinders, whose radius and angular velocities are r_i^*, r_o^* and Ω_i, Ω_o respectively. The annular gap between the cylinders is $d = r_o - r_i$. In addition, the inner cylinder is moving parallel to the common axis with a constant velocity U_c (see figure 1). The apparently more general flow with both cylinders moving axially is reduced to the present case by Galilean invariance, changing to a reference frame with constant axial speed.

The independent non-dimensional parameters appearing in this problem are: the radius ratio $\eta = r_i^*/r_o^*$, which fixes the geometry of the annulus; the Couette flow Reynolds numbers $R_i = dr_i\Omega_i/\nu$ and $R_o = dr_o\Omega_o/\nu$ of the rotating cylinders and the axial Reynolds number $R_z = dU_c/\nu$ measuring the translational velocity of the inner cylinder.

Henceforth, all variables will be rendered dimensionless using d, d^2/ν, ν^2/d^2 as units for space, time and the reduced pressure (p^*/ρ^*). The Navier–Stokes equation and the incompressibility condition for this scaling become

$$\partial_t \boldsymbol{v} + (\boldsymbol{v}\cdot\nabla)\boldsymbol{v} = -\nabla p + \Delta\boldsymbol{v}, \quad \nabla\cdot\boldsymbol{v} = 0. \tag{2.1}$$

Let (u, v, w) be the physical components of the velocity $\boldsymbol{v}$ in cylindrical coordinates (r, θ, z). The boundary conditions for the flow described above are

$$u(r_i) = u(r_o) = 0, \tag{2.2}$$

$$v(r_i) = R_i, \quad v(r_o) = R_o, \tag{2.3}$$

$$w(r_i, t) = R_z, \quad w(r_o) = 0, \tag{2.4}$$

where $r_i = \eta/(1-\eta)$, $r_o = 1/(1-\eta)$.

In order to compare with experiments and also with some previous work, two different situations are considered in this paper. In both, the basic flow velocity field is independent of the axial direction, but in one case the axial pressure gradient is zero (*open flow*) and non-zero in the other (*enclosed flow*). The non-zero axial pressure gradient in the enclosed flow case represents the presence of endwalls and allows us to enforce a net zero axial mass flux, not only for the base flow but also for the perturbed flow. The only experiments on the Taylor–Couette flow with axial sliding of the inner cylinder known to us are those of Ludwieg (1964) which were carried out in an annulus with open endwalls. The use of an axial pressure gradient to include the large-scale endwall effects has been implemented by Ali & Weidman (1993) in the linear analysis of Taylor–Couette flow with axial sliding, in the enclosed case and with the outer cylinder at rest. This effect was also taken into account by Edwards *et al.* (1991) and Sanchez, Crespo & Marques (1993) in Couette flow without sliding, where the bifurcation to spirals in the counter-rotating case develops weak axial flows. The axial pressure gradient is fixed by the zero axial mass flow condition

$$\int_{z=0} w\, r\, \mathrm{d}r\, \mathrm{d}\theta = 0. \tag{2.5}$$

The steady velocity field $\boldsymbol{v}_B$ independent of the axial and azimuthal variables that verifies the previous condition is

$$u_B = 0, \qquad v_B = Ar + B/r, \qquad w_B = C\ln(r/r_o) + P(r^2 - r_o^2)/4, \tag{2.6}$$

as can be seen in Joseph (1976). The constants A, B, C are given by

$$A = \frac{R_o - \eta R_i}{1+\eta}, \qquad B = \frac{\eta(R_i - \eta R_o)}{(1-\eta)(1-\eta^2)}, \qquad C = \frac{1}{\ln\eta}\left(R_z + \frac{P(1+\eta)}{4(1-\eta)}\right) \tag{2.7}$$

and P is the non-dimensional Poiseuille number $P = (\mathrm{d}p^*/\mathrm{d}z^*)d^3/(\rho^* v^2)$ measuring the axial pressure gradient imposed. In the open flow case, $P = 0$; in the enclosed case, the mass conservation condition gives P as a function of R_z:

$$P = -4R_z \frac{(1-\eta)(2\eta^2\ln\eta + 1 - \eta^2)}{(1+\eta)[(1+\eta^2)\ln\eta + 1 - \eta^2]}. \tag{2.8}$$

3. Linear stability of the basic flow

In the preceding section the basic flow was obtained. We now perturb this basic state by a small disturbance which is assumed to vary periodically in the azimuthal and axial directions:

$$\boldsymbol{v}(r,\theta,z,t) = \boldsymbol{v}_B(r) + \mathrm{e}^{\mathrm{i}(n\theta+kz)+\lambda t}\boldsymbol{u}(r), \tag{3.1}$$

$$p(r,\theta,z,t) = p_B(r,z) + p'(r)\mathrm{e}^{\mathrm{i}(n\theta+kz)+\lambda t}, \tag{3.2}$$

where $\boldsymbol{v}_B = (0, v_B, w_B)$ is given by (2.6) and the boundary conditions for $\boldsymbol{u}$ are homogeneous, $\boldsymbol{u}(r_i) = \boldsymbol{u}(r_o) = \boldsymbol{0}$. Linearizing the Navier–Stokes equations about the basic solution, we obtain the eigenvalue problem

$$\lambda\boldsymbol{u} = -\nabla p' + \Delta\boldsymbol{u} - \boldsymbol{v}_B\cdot\nabla\boldsymbol{u} - \boldsymbol{u}\cdot\nabla\boldsymbol{v}_B. \tag{3.3}$$

The spatial discretization of the problem, in order to solve (3.3) numerically, is accomplished by projecting (3.3) onto a suitable basis. The space of divergence-free vector fields satisfying the boundary conditions of the problem is

$$V = \{\boldsymbol{u} \in (\mathscr{L}_2(r_i, r_o))^3 \mid \nabla \cdot \boldsymbol{u} = 0,\ \boldsymbol{u}(r_i) = \boldsymbol{u}(r_o) = 0\}, \tag{3.4}$$

where $(\mathscr{L}_2(r_i, r_o))^3$ is the Hilbert space of square-integrable vectorial-functions defined in the interval (r_i, r_o), with the inner product

$$\langle \boldsymbol{u}, \boldsymbol{v} \rangle = \int_{r_i}^{r_o} \boldsymbol{u}^* \cdot \boldsymbol{v}\ r \mathrm{d}r, \tag{3.5}$$

where * denotes the complex conjugate. For any $\boldsymbol{u} \in V$ and any function p, we have $\langle \boldsymbol{u}, \nabla p \rangle = 0$. Therefore expanding $\boldsymbol{u}$ in a suitable basis of V

$$\boldsymbol{u} = \sum_{\alpha} a_\alpha \boldsymbol{u}_\alpha, \qquad \boldsymbol{u}_\alpha \in V, \tag{3.6}$$

and projecting the linearized equations (3.3) onto V the pressure term disappears, and we get a linear system for the coefficients a_α:

$$\lambda \sum_{\beta} \langle \tilde{\boldsymbol{u}}_\alpha, \boldsymbol{u}_\beta \rangle a_\beta = \sum_{\beta} \langle \tilde{\boldsymbol{u}}_\alpha, \Delta \boldsymbol{u}_\beta - \boldsymbol{v}_B \cdot \nabla \boldsymbol{u}_\beta - \boldsymbol{u}_\beta \cdot \nabla \boldsymbol{v}_B \rangle a_\beta. \tag{3.7}$$

We implement a Petrov–Galerkin scheme, where the basis used to expand the unknown velocity, $\{\boldsymbol{u}_\alpha\}$, differs from that used to project the equations, $\{\tilde{\boldsymbol{u}}_\alpha\}$. A comprehensive analysis of the method can be found in Moser, Moin & Leonard (1983) or Canuto *et al.* (1988). The divergence-free condition for a velocity field of the form (3.1) is $\mathrm{D}_+ u + \mathrm{i}nv/r + \mathrm{i}kw = 0$, and a basis for V is obtained by taking

$$\boldsymbol{u}_j^1 = (0, -rkh_j(r), nh_j(r)), \tag{3.8}$$

$$\boldsymbol{u}_j^2 = (-\mathrm{i}kf_j(r), 0, \mathrm{D}_+ f_j(r)), \tag{3.9}$$

where $\mathrm{D} = \partial_r$, $\mathrm{D}_+ = \mathrm{D} + 1/r$. The functions f_j and h_j must satisfy the homogeneous boundary conditions $f_j = f_j' = h_j = 0$ on r_i and r_o.

Introducing the new radial coordinate $x = 2(r - r_i) - 1$, $x \in [-1, +1]$ and using Chebyshev polynomials T_j, a simple choice for f_j and h_j, which satisfies the homogeneous boundary conditions, is

$$f_j(r) = (1 - x^2)^2 T_{j-1}(x), \quad h_j(r) = (1 - x^2) T_{j-1}(x), \tag{3.10}$$

where j ranges from 1 to M, the number of Chebyshev polynomials used. In order to preserve the orthogonality relationships between the Chebyshev polynomials, and to avoid $1/r$ factors in the inner products in (3.7), a suitable choice for the projection basis $\tilde{\boldsymbol{u}}$ is

$$\tilde{f}_j(r) = r^2 (1 - x^2)^{3/2} T_{j-1}(x), \quad \tilde{h}_j(r) = r^2 (1 - x^2)^{1/2} T_{j-1}(x). \tag{3.11}$$

With this choice, all the inner products in (3.7) involve polynomials, except those containing the logarithmic term in w_B, and therefore can be numerically computed exactly using Gauss–Chebyshev quadrature (Isaacson & Keller 1966). Finally we obtain a generalized eigenvalue system of the form

$$\lambda \boldsymbol{G} \boldsymbol{x} = \boldsymbol{H} \boldsymbol{x}, \tag{3.12}$$

where the vector $\boldsymbol{x}$ contains the real and imaginary parts of the coefficients a_α in (3.6), and $\boldsymbol{G}$, $\boldsymbol{H}$ are constant matrices, with $\boldsymbol{G}$ positive definite. The explicit expressions for the matrix elements of $\boldsymbol{G}$ and $\boldsymbol{H}$ are given in the Appendix A.

Let us consider the symmetries of our problem. The Navier–Stokes equations are invariant with respect to the specular reflections $\{z \to -z,\ w \to -w\}$ and $\{\theta \to -\theta,\ v \to -v\}$. They are also invariant with respect to rotations around the axis, axial translations and time translations. The boundary conditions break some of these symmetries. R_i or R_o different from zero breaks the specular reflection $\theta \to -\theta$, and $R_z \neq 0$ breaks the specular reflection $z \to -z$. In order to keep the invariance we must change the sign of these Reynolds numbers, and of the corresponding wavenumbers n and k in the solutions of the linearized system (3.12). Therefore the symmetries allow us to restrict the computations to the cases $R_z > 0$ and $R_i > 0$. Furthermore, since the Navier–Stokes equations are real, the complex conjugate of a perturbation (3.1), (3.2) is also a solution, and we can change simultaneously the sign of n, k and the imaginary part of λ. Then we can restrict the computations to the case $k \geqslant 0$.

When n and k are non-zero, the eigenvector of the linear problem has the form of a spiral pattern (see figure 12*a*, showing an experimentally observed spiral flow). The wavenumbers n and k, together with the imaginary part of the critical eigenvalue, $\omega = \operatorname{Im}\lambda$, fix the shape and speed of the spiral. The angle α of the spiral with a constant-z plane is given by $\tan\alpha = -n/(r_o k) = -(1-\eta)n/k$; the speed of the spiral in the axial direction (on a constant-θ line) is $c = -\omega/k$, and in the azimuthal direction (on a constant-z line) it is $\omega_{sp} = -\omega/n$. In the $n = 0$ case the pattern is axisymmetric and we have steady Taylor vortices if $\omega = 0$ and travelling Taylor vortices if $\omega \neq 0$, with axial velocity c.

If $R_z = 0$, the symmetry $z \to -z$ is not broken, and at the bifurcation point, in the $n \neq 0$ case, we get two pairs of purely imaginary eigenvalues bifurcating at the same time, representing spirals with opposite slope – or angle – (see Chossat & Iooss 1994). These spirals have opposite values of n. For $R_z \neq 0$, the corresponding eigenvalues split apart, and one of the two spirals $\pm n$ becomes dominant. Therefore we expect mode competition and switching between $+n$ and $-n$ for R_z close to zero.

3.1. *Computation of the neutral stability curves*

Let σ be the real part of the first eigenvalue of the linear system (3.12) which crosses the imaginary axis. The stability of the basic flow is determined by the sign of σ. For negative values of σ, the basic flow is stable under perturbations. When σ is zero or slightly positive, the steady flow becomes unstable and bifurcated secondary flows may appear. It should be remarked that $\sigma(n, k, \eta, R_i, R_o, R_z)$ is a function of the physical parameters which play an essential role in the dynamics of the system. For fixed η, R_o, R_z, and given n, k, the inner Reynolds number $Ri_c(n,k)$ such that $\sigma = 0$ is computed. The critical inner Reynolds number is given by $Ri_{\text{crit}} = \min_{n,k} Ri_c(n,k)$, and the corresponding values of n, k are the critical azimuthal and axial wavenumbers n_{crit}, k_{crit} which will dictate the geometrical shape of the critical eigenfunction, which may be a spiral flow or travelling Taylor vortices. Furthermore, the imaginary part of the critical eigenvalue, ω_{crit}, gives the angular frequency of the critical eigenfunction. Again, the critical values are functions of the parameters (η, R_o, R_z).

The curves in the (k, R_i)-plane given by $\sigma(k, R_i) = 0$ are commonly termed neutral stability curves (NSC). The main goal at this stage is to compute the absolute minimum of the NSC, which will give the critical parameters $(k_{\text{crit}}, R_{i\text{crit}})$ – in fact, the absolute minimum of the set of the NSC corresponding to integer values of n will be found. As will be seen later, the NSC curves for this problem may have multiple extrema (maxima and minima), and exhibit disconnected parts and sharp geometrical forms. Furthermore, these curves may exhibit multivalued branches as functions of k, and these features can change abruptly in some parameter ranges

N	R_{ic}	k_c
8	495.9915 1881	3.0906 0924
16	496.6464 3476	3.3000 7171
24	496.6466 5308	3.3001 3843
32	496.6466 3840	3.3001 3305
40	496.6466 3825	3.3001 3014
48	496.6466 3825	3.3001 3300

TABLE 1. Critical values as a function of the spectral approximation order. These values have been evaluated for the specific case $\eta = 0.5$, $R_o = 250.0$ and $R_z = 50.0$, $n = -1$ being the dominant azimuthal wavenumber.

(see figure 3). Standard methods applied to a regular grid in the plane (k, R_i) require exorbitantly high-accuracy computations. Consequently, an alternative method has been considered.

A local extremum (k_c, R_{ic}) must satisfy the following conditions:

$$\sigma(k_c, R_{ic}) = 0, \quad \partial_k \sigma(k_c, R_{ic}) = 0. \tag{3.13}$$

Using the implicit function theorem, it can be seen that the local extremum is a minimum if, in addition, the inequality $(\partial^2_{k,k}\sigma)(\partial_{R_i}\sigma) < 0$ is satisfied. In order to solve equation (3.13), a two-dimensional Newton–Raphson method is used. The convergence of the method depends on the topological structure of the basin of attraction of the different minima sought by the Newton method, and is strongly dependent on the initial point of iteration in the plane (k, R_i). In order to optimize the process, a predictor steepest-descent method has been employed. This gradient method allows computations to reach the neighbouring zones where the convergence is almost ensured. The predictor scheme is able to detect islands of instability independently of their size and topological features.

In order to check the feasibility of the computational method, a numerical test was carried out. For this purpose, specific critical values were computed for a different number of spectral modes. The convergence of the numerical method is reflected in table 1, where the critical inner Reynolds number R_{ic} and the critical axial wavenumber k_c are presented as a function of the number of the spectral modes (N) considered for their computation in each case. Other critical parameters, like ω, behave similarly. The results presented correspond to the $\eta = 0.5$ case, although we have also checked the convergence in the $\eta = 0.8$ case, particularly for the parameter values corresponding to Ludwieg's experiments (Ludwieg 1964), obtaining the same behaviour. Throughout this work, the number of modes used for the computation of the linear stability regime was $N = 24$, which provided seven exact figures in the critical Reynolds number and five exact figures in the critical axial wavenumber.

3.2. *Comparison between open and enclosed flows* ($R_o = 0$)

In order to check the numerical scheme, the linear stability of the open and enclosed flows has been studied for $\eta = 0.4$ and a stationary outer cylinder ($R_o = 0$).

For the enclosed flow case, the present computations are in complete agreement with the results of Ali & Weidman (1993). The numerical results are displayed in figure 2. For high axial sliding Reynolds number, the azimuthal dominant mode is $n = 4$, as was predicted previously by Ali & Weidman (1993).

In order to study the effect of a non-zero mean flow, the same computations have

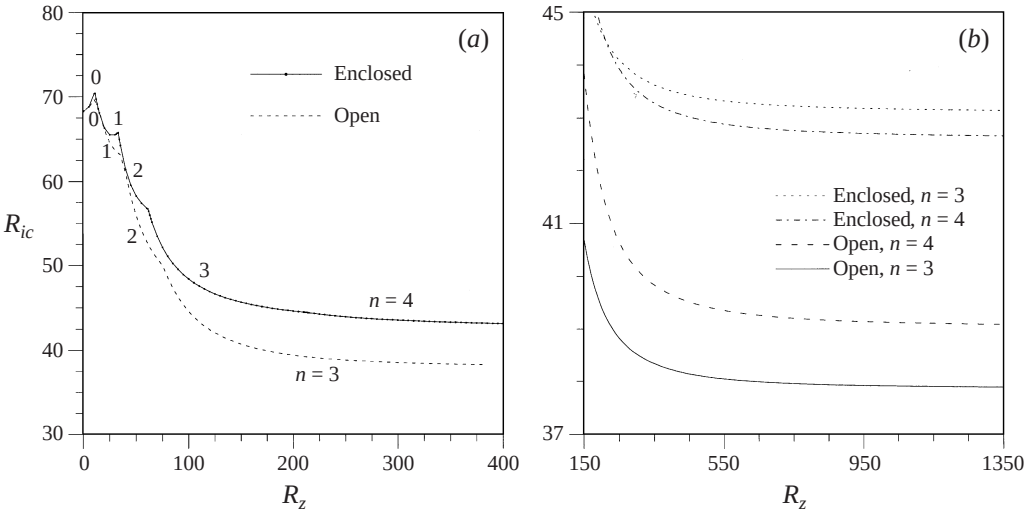

FIGURE 2. Comparison between the open and enclosed cases for $\eta = 0.4$ and $R_o = 0$; the critical R_{ic} is shown as a function of R_z. (*a*) The dominant azimuthal wavenumber is indicated in each curve segment. (*b*) Asymptotic states for high axial Reynolds number R_z.

been performed for the open-flow configuration. The qualitative behaviour of the system is similar to the zero mean flow case, but some quantitative differences can be pointed out. First, the global end effects included in the enclosed case have a stabilizing effect on the basic flow, an effect that increases at high axial Reynolds number (see figure 2*a*). This enhancement of stability in the enclosed case is similar to the one observed by Marques & Lopez (1997) when the inner cylinder undergoes axial oscillations. Second, the asymptotic azimuthal wavenumber n is different, being the dominant azimuthal wavenumber $n = 3$ in the open case, and $n = 4$ in the enclosed one, in agreement with Ali & Weidman (1993) (see figure 2*b*). According to equation (3.2), the azimuthal wavenumber in figure 2 should be negative, but we have adopted here the Ali & Weidman prescription for comparison; they used $e^{i(kz-n\theta)}$ instead of (3.2).

Nevertheless, only the open-flow configuration will be considered henceforth. In fact, all the previous experiments have been performed using the open axial circulation configuration. We have computed the inner-cylinder critical rotation Reynolds number R_{icrit} as a function of (R_z, R_o) for two different values of η, 0.5 and 0.8. This has been done in the range $0 < R_z < 150$ and $-250 < R_o < 250$. We have restricted the computations to the cases $R_z > 0$, $R_i > 0$ and $k > 0$, on the basis of the symmetries of the physical problem.

4. Instability results for $\eta = 0.5$

The computation of $R_{ic}(R_z, R_o)$ for the wide gap $\eta = 0.5$, gives as a first striking result the presence of a zeroth-order discontinuity in R_{ic}, in the co-rotating case ($R_o > 0$). Although this behaviour has been considered possible by some authors (Davis & Rosenblat 1977), specific examples showing this kind of discontinuity are very unusual in the fluid mechanics literature.

For $R_o = 200$ the discontinuity appears for $R_z = 82.63$. We show in figure 3(*a*) the critical R_i as a function of k. For $R_z = 80$ the dominant mode is $n = -1$,

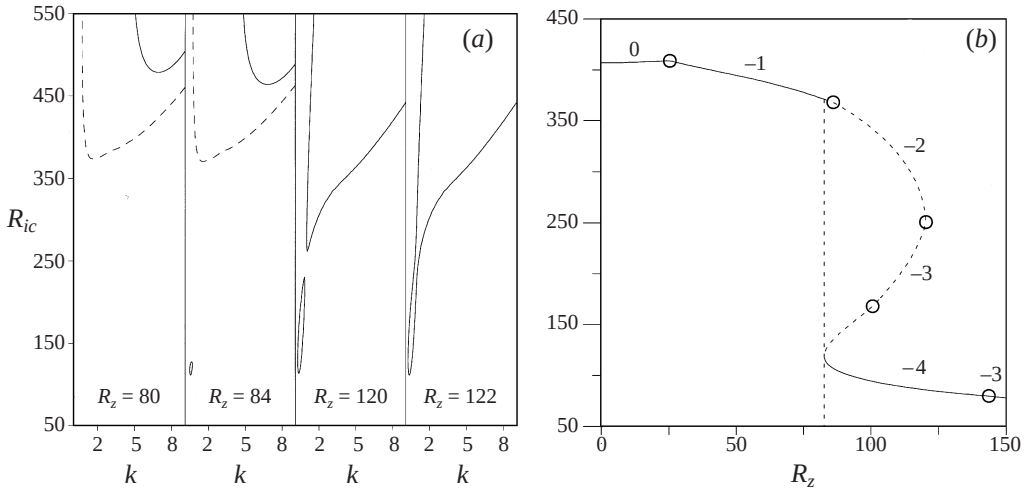

FIGURE 3. (*a*) Formation and evolution of an island of instability for $\eta = 0.5$, $R_o = 200$. The solid line corresponds to the $n = -4$ mode, and the dashed one to $n = -1$. (*b*) The corresponding critical inner Reynolds number R_{ic} as a function of R_z (solid line); the dashed line is a section ($R_o = 200$) of the critical surface (figure 5). The labels refer to the dominant azimuthal mode number n; the circles are the transitions between different n. R_{ic} is discontinuous for $R_z = 82.64$.

giving $R_{ic} = 373.43$ and $k_c = 1.68$; but for $R_z = 82.63$ the marginal stability curve of the $n = -4$ mode develops an island of instability for a much lower $R_{ic} = 119.13$, introducing a discontinuity in R_{ic}. Notice too that the change by n_{crit} is not ± 1 as usual, but it changes by three units. The island of instability is very small (figure 3*a*, $R_z = 84$), becoming larger when we move away of the discontinuity. All these features make the numerical computation of the critical parameters very difficult from the algorithmic point of view. For these reasons we have developed specific numerical methods, outlined in § 3.1, in order to detect the islands as soon as they appear. Similar islands of instability have been found in McFadden *et al.* (1990) and Marques & Lopez (1997).

Before crossing the R_{ic} discontinuity, the marginal stability curve for $n = -4$ has a single extremum, a minimum (figure 3*a*, $R_z = 80$), giving the critical parameter values (R_{ic}, k_c). After crossing, and due to the appearance of the island, we have three extrema, two minima and a maximum, and the marginal stability curve has two disconnected branches. If we move to higher R_z values, the island grows until it merges with the other branch (figure 3*a*, $R_z = 120$, 122); the marginal curve has now a single minimum. Plotting the position of all the extrema as a function of R_z, we get an S-shaped curve, displayed in figure 3(*b*); the solid curve gives the absolute minimum, and the dashed curve corresponds to the other extrema. The critical Reynolds number R_{ic} becomes discontinuous (zeroth-order discontinuity) as soon as the island of instability appears for $R_z = 82.64$; experiments with increasing R_i and R_z held fixed would give the solid curve in figure 3(*b*). Nevertheless, this curve is smooth except for the presence of discontinuities in the derivative (first-order discontinuities), which appear when the critical azimuthal wavenumber changes (bicritical points, marked with circles). The whole critical surface is multivalued and continuous, but is folded in such a way that a cusp develops; figure 4(*a*) shows a perspective view of the critical surface. Figure 4(*b*) shows the same critical surface with the curves corresponding to a change in the critical azimuthal wavenumber

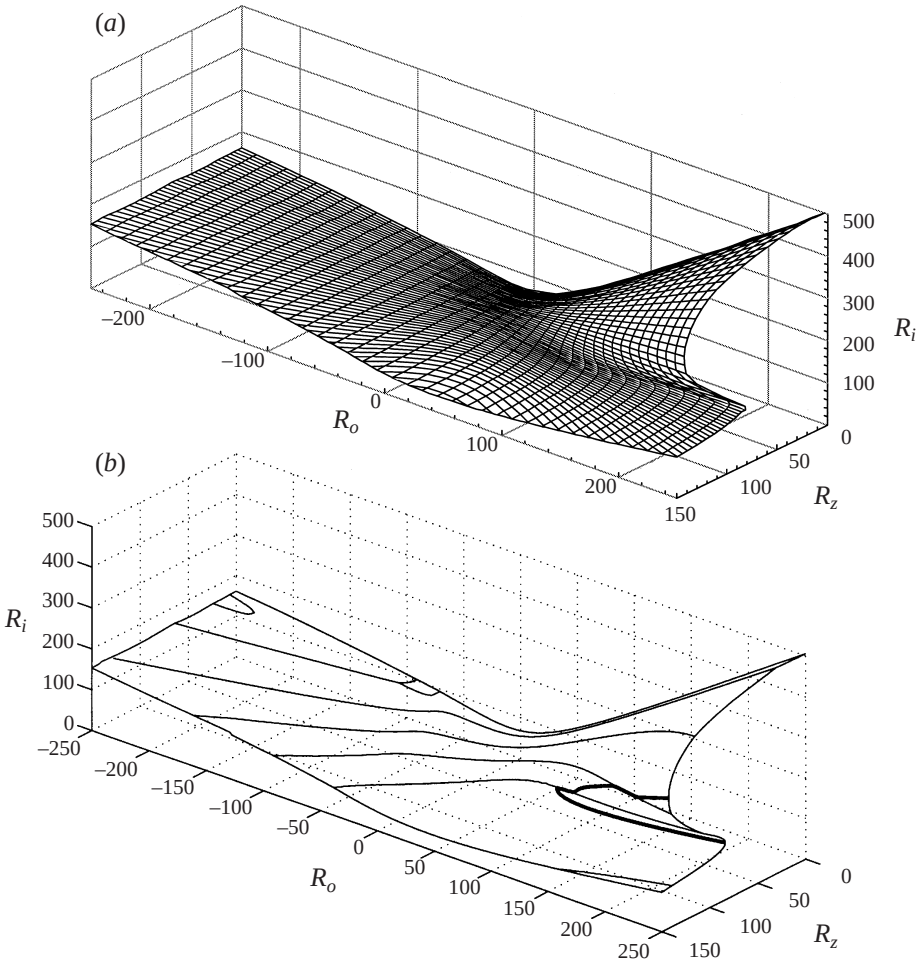

FIGURE 4. (*a*) Perspective view of the critical surface $R_{ic}(R_o, R_z)$ for $\eta = 0.5$. (*b*) Same view, explicitly showing the changes in the dominant azimuthal mode n at criticality. The edges of the cusp region are also plotted as thick lines.

n, where the surface is not smooth (the tangent plane is discontinuous along these curves).

The discontinuity of the critical parameter depends on the experimental conditions. If we had fixed R_i and computed $R_{zc}(R_i, R_o)$, we would have found a continuous surface, formed by all three sheets in the cusp region. This is the way we have followed in order to obtain the critical surface in the cusp region, because the critical wavenumber n can also change (see figure 3*b*). As stated in the introduction, for dynamical systems depending on a sufficient number of parameters, the critical surface (a manifold, in the general case) is likely to present discontinuities of the same kind, or more complex. As we lack *a priori* knowledge of this possibility, the use of robust strategies, like those we have implemented, to find the critical points becomes necessary.

The projection of the curves corresponding to a change in the azimuthal wavenumber n are plotted in figure 5. We see that along these curves, the change in n_{crit} is always ± 1, except very close to the $R_z = 0$ axis, where the competition between

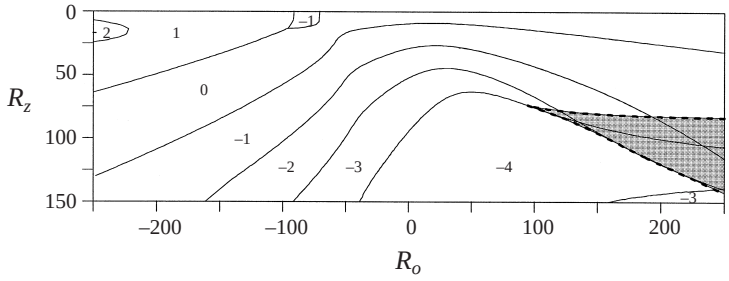

FIGURE 5. Dominant azimuthal mode n at criticality, as a function of R_o, R_z; $\eta = 0.5$. The shaded region corresponds to the fold, whose edges are plotted as thick dashed lines.

modes $\pm n$ is strong. As we have already mentioned, the symmetries of the problem for $R_z = 0$ makes the eigenvalues corresponding to $\pm n$ bifurcate simultaneously. When the symmetry breaking is small ($R_z \sim 0$), both eigenvalues are very close, and there is switching between both critical surfaces close to the axis; see direct changes between modes -2 and $+1$, and -1 and $+1$, close to the $R_z = 0$ axis in figure 5. In the region of the cusp, near the discontinuity in R_{ic}, the change in n_c is also large, because we jump between the different sheets of the critical surface; but if we continuously move on the critical surface, the change is n_c is also ± 1. This is clearly seen in figure 3(*b*).

The edges of the cusp region are plotted as thick lines in both figures 4(*b*) and 5. The discontinuity in R_{ic} corresponds to the upper edge of the fold region, and inside it the dominant azimuthal wavenumber is $n = -4$, except at the very end ($R_o \sim 250$) where the mode $n = -3$ becomes dominant.

The coordinates of the cusp point are $R_o = 93.22$, $R_z = 73.41$, $R_{ic} = 107.63$, inside the region $n_c = -3$, but very close to the border with $n = -4$. Although we could think of this cusp point as being a bifurcation point of codimension higher than 1, it is *not*. The cusp point is characterized by having a tangent plane parallel to the R_i-axis, simultaneous with an inflection point in the R_o-constant section. But if we look at the critical surface from another point of view (for example changing R_i to a linear combination of the Reynolds numbers, as for experimental purposes), the cusp point changes its position on the surface. In fact, looking for the critical R_z with R_i, R_o fixed, all the folding region is now single-valued, and R_z is continuous there. In this case we *also* have discontinuities (in R_z) and a multivalued critical surface, but now in a different region of the critical surface. Figure 7(*a*) shows that close to $R_z = 0$, when the $n = 0$ mode is dominant, R_{ic} slightly increases with R_z, but decreases for higher R_z when $n \neq 0$. Therefore R_z is multivalued, and a discontinuity appears. These discontinuities and fold structure may have important consequences which could be detected experimentally, like hysteresis phenomena, as well as the discontinuity in R_{ic}.

Figure 6 shows R_{ic}, ω_c, α and c as a function of R_o for different values of R_z. The critical Reynolds number R_{ic} (figure 6*a*) is almost independent of R_z in the counter-rotating region $R_o < 0$. But in the co-rotating region, where the cusp develops, we have two well-separated kinds of behaviour. This figure is a front view of the cusp structure (figure 4) along the R_z-axis. For small axial sliding R_z, before the discontinuity, R_{ic} is very close to the values without sliding (Taylor–Couette flow). For higher axial sliding, after the discontinuity, R_{ic} falls to much lower values. The axial sliding is always destabilizing, but its effect becomes significant only in the co-rotating case, after the discontinuity. The centrifugal instability seems the dominant mechanism (as in Taylor–Couette, $R_z = 0$) except after the discontinuity, where a shear instability

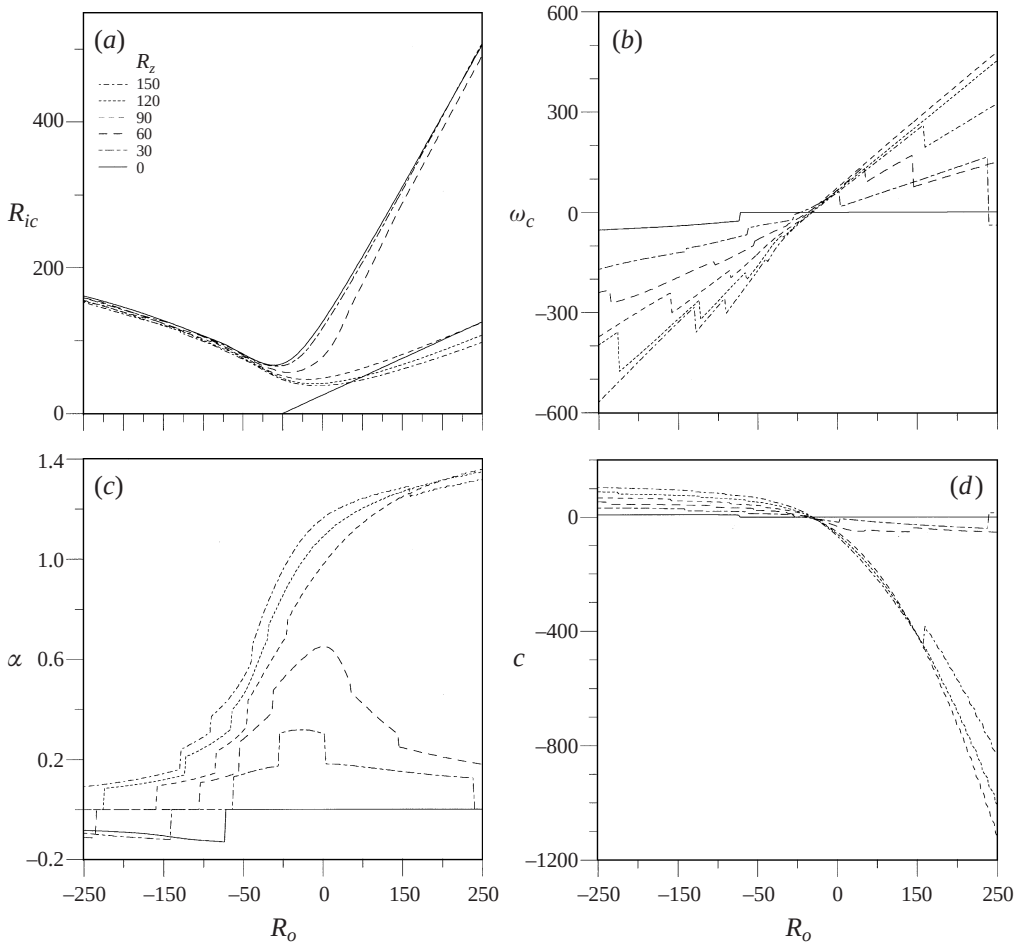

FIGURE 6. Critical parameters for $\eta = 0.5$, as functions of the outer Reynolds number R_o. (*a*) Critical inner Reynolds number R_{ic}; the solid straight line is the rigid rotation line $R_i = \eta R_o$. (*b*) Imaginary part of the critical eigenvalue ω_c. (*c*) Angle of the spiral pattern α in radians. (*d*) Axial pattern velocity c.

due to the axial sliding becomes dominant; the cuspidal zone can be thought as the transition region between both mechanisms. This qualitative change can also be noticed in the angle of the spiral pattern α (figure 6*c*), which jumps from values less than 0.2 radians (10°) to values close to 1.2 radians (70°). This dramatic change in shape is reflected too in the axial speed of the spirals, in figure 6(*d*). We have presented our results in terms of α and c instead of k because these variables are easy to measure experimentally and better discriminate between the two mechanisms; the k value can be immediately obtained by using the expression $k = -\omega/c$. We also notice that the shear-instability-dominated branch is very close to the solid-body rotation line (see figure 6*a*), where the centrifugal instability does not play a significant role; see detailed comments in § 4.1.

The angular velocity of the spiral pattern, ω_c, which is the imaginary part of the critical eigenvalue, is displayed in figure 6(*b*). It changes in a linear way with R_o, except for jumps when the azimuthal mode n changes. Looking at figure 5, we see that the azimuthal wavenumber n decreases when R_z increases, except in two regions: the first

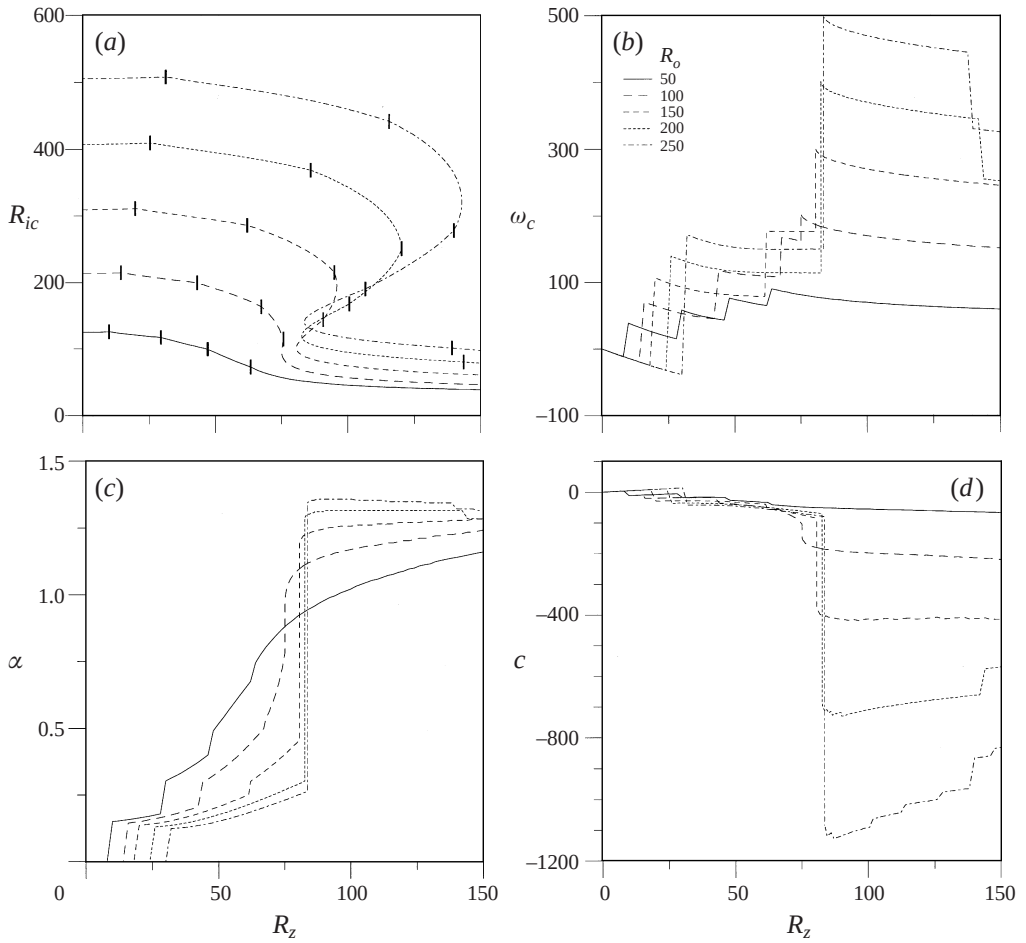

FIGURE 7. Critical parameters for $\eta = 0.5$, as functions of the axial Reynolds number R_z in the co-rotating case $R_o > 0$. (*a*) Critical inner Reynolds number R_{ic}; the bars mark the change in the critical azimuthal mode n. (*b*) Imaginary part of the critical eigenvalue ω_c. (*c*) Angle of the spiral pattern α in radians. (*d*) Axial pattern velocity c.

one, close to $R_z = 0$ in the counter-rotating area, displays competition between $\pm n$ modes, due to the breaking of the reflectional symmetry $z \to -z$, as described in § 3; the second region, after the discontinuity, shows a kind of saturation – the azimuthal $n = -4$ mode is dominant in a very large area.

Figure 7 shows R_{ic}, ω_c, α and c as a function of R_z for different values of R_o in the co-rotating case. In figure 7(*a*) sections of the cusp region are displayed; the critical R_{ic} is in fact the minimum of the values in the multivalued region, so we have a discontinuity which grows when increasing R_o. The discontinuity has been displayed in the remaining critical parameter plots, figure 7(*b*, *c*, *d*). The bicritical points where the azimuthal wavenumber n changes and two eigenvalues bifurcates simultaneously are distinguished with a vertical bar. The dominant mode for small sliding (R_z close to zero) is axisymmetric $n = 0$, and when the imaginary part of the critical eigenvalue is not zero (except for $R_o = 0$, see figure 7*b*), we have Taylor vortices travelling axially with a speed c as shown in figure 7(*d*). The effect of the sliding on these axisymmetric modes is slightly stabilizing, in contrast to their destabilizing effect on

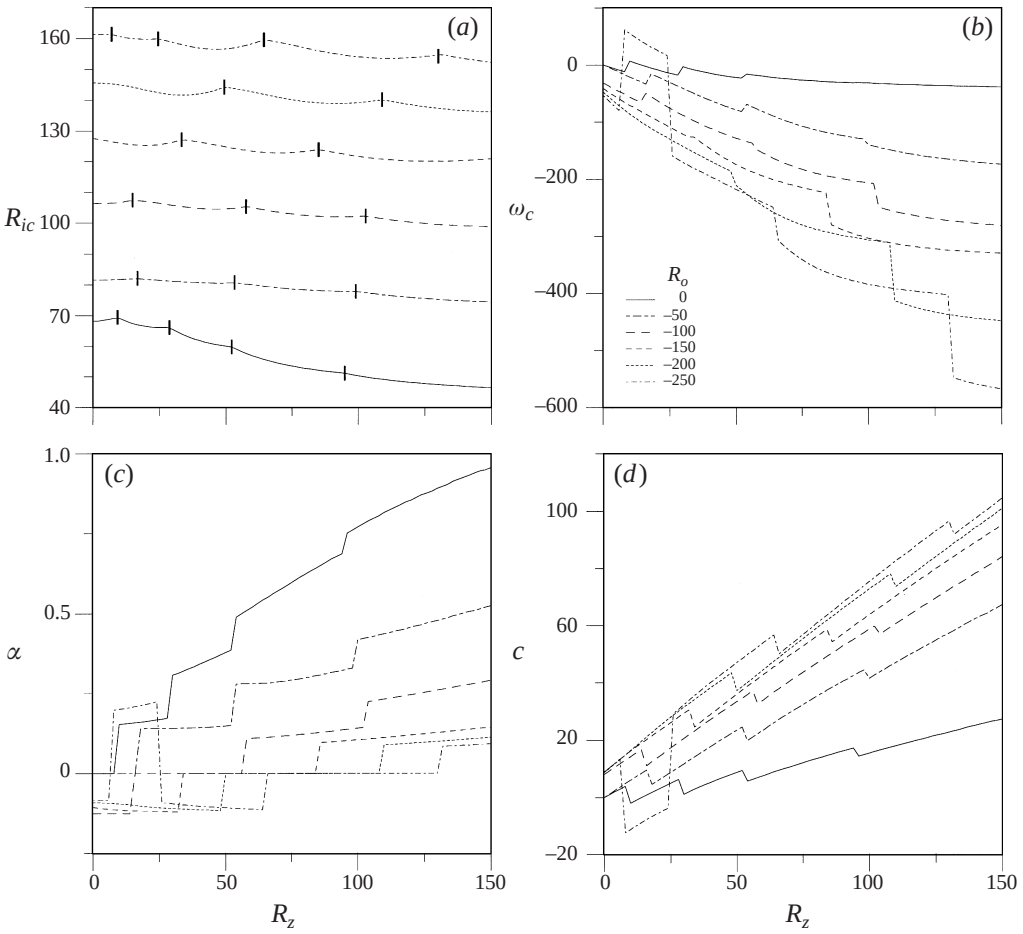

FIGURE 8. Critical parameters for $\eta = 0.5$, as functions of the axial Reynolds number R_z in the counter–rotating case $R_o < 0$. (*a*) Critical inner Reynolds number R_{ic}. (*b*) Imaginary part of the critical eigenvalue ω_c. (*c*) Angle of the spiral pattern α. (*d*) Axial pattern velocity c.

the non-axisymmetric modes, mainly in the co-rotating region, an effect also reported by Ali & Weidman (1993).

Figure 8 shows R_{ic}, ω_c, α and c as a function of R_z for different values of R_o in the counter-rotating case. Here all the critical parameters change smoothly, in an almost linear way. Figure 8(*a*) shows that the critical Reynolds number R_{ic} is almost independent of the axial sliding R_z for $R_o < 0$, suggesting that the centrifugal instability is the dominant instability mechanism as has been noticed before.

4.1. *Axial sliding with rigid rotation* ($R_i = \eta R_o$)

In this section we analyse the rigid rotation case $\Omega_i = \Omega_o$ (or equivalently $R = R_i = \eta R_o$) with sliding because it is relevant to understanding the dominant instability mechanism in the cusp region. This situation is also interesting because of its linear stability for both limiting cases $R_z = 0$, $R = 0$. The situation is very similar to Mackrodt (1976) where it is shown that although the Poiseuille flow in a circular pipe is linearly stable for any Reynolds number, adding a slow rotation of the pipe makes the flow unstable at some finite Reynolds number. And conversely, the rigid rotation

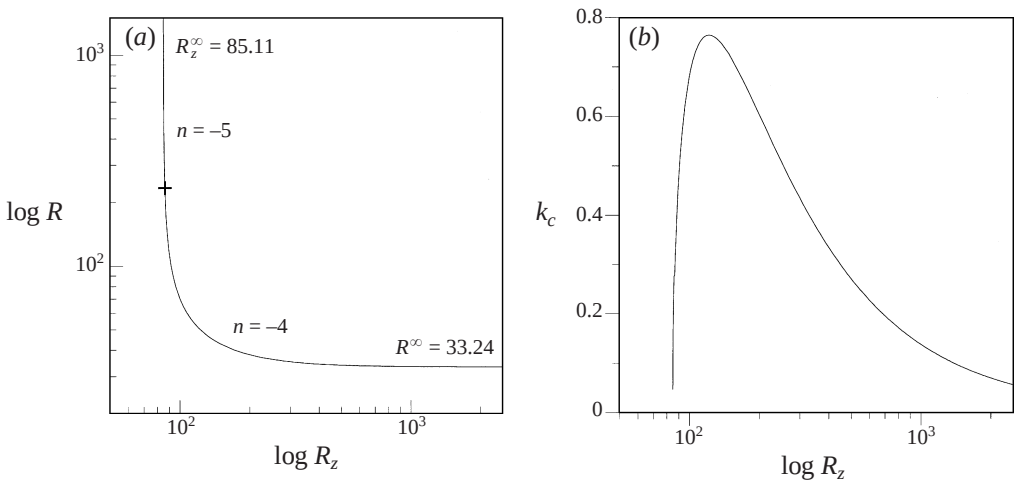

FIGURE 9. Sliding rigid rotation. (*a*) Critical rotation number $R = R_i = \eta R_o$ and (*b*) critical wavenumber k as a function of the axial speed R_z.

flow in a circular pipe is linearly stable, but adding a finite axial pressure gradient makes the flow unstable.

Figure 9 shows the computed critical rotation number $R = R_i = \eta R_o$ and critical wavenumber k as a function of the axial speed R_z. The critical regime has an asymptotic value as R_z is increased, being the asymptotic rotation Reynolds number $R^\infty = 33.24$. In this limit, the critical azimuthal mode is $n = -4$. On the other hand, as the rotation Reynolds number increases, R_z approaches another asymptotic value which is $R_z^\infty = 85.11$, with a critical azimuthal wavenumber $n = -5$. The dependence of the critical axial wavenumber k_c on the marginal curve is depicted in figure 9(*b*). We can observe the presence of a maximum for the values $R_z = 122.05$, $R_i = 50.25$, $k_{max} = 0.7638$. Figures 9(*a*) and 9(*b*) are very similar to figures 1 and 3 in Mackrodt (1976), where the same problem but without the inner cylinder is considered. Figure 9(*b*) shows that the critical wavenumber k decreases to very low values (less than 0.1) as the axial Reynolds number R_z increases; as a result, the spiral's slope grows. This behaviour completely agrees with the splitting observed in figure 7(*c*) between the centrifugal (small α) and shear (large α) dominated flows.

Therefore, in the co-rotation region, when we increase the inner Reynolds number R_i and prior to the onset of centrifugal instability, the solid-body rotation line (figure 6*a*) must be traversed. If also R_z is greater than 85.11, the shear instability comes into play: the lower part of the cusp appears, giving a discontinuous Reynolds number with shear dominating the centrifugal instability mechanism. The corresponding eigenfunctions are clearly different from the centrifugally dominated ones. Now the axial wavenumber k is very small, giving large spiral angles α, and an almost constant azimuthal wavenumber n (equal to -4). The cuspidal zone, where the critical surface is multivalued, corresponds to the competition between the centrifugal instability mechanism (upper branch) and the shear instability mechanism (lower branch), continuously connected by the intermediate sheet. All three branches can be experimentally observed if we fix R_i and steadily increase the axial Reynolds number R_z.

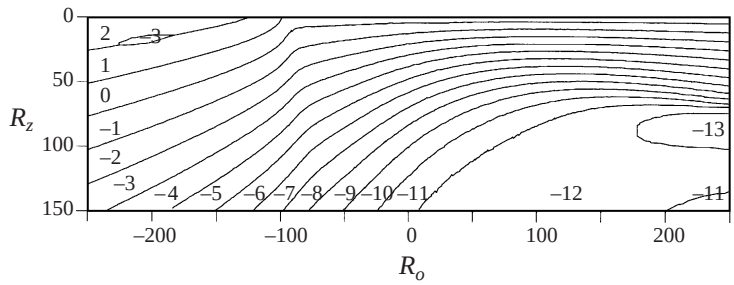

FIGURE 10. Dominant azimuthal mode n at criticality, as a function of R_o, R_z; $\eta = 0.8$.

5. Instability results for $\eta = 0.8$

The qualitative features of the critical surface for $\eta = 0.8$ are the same as those in the wide gap case $\eta = 0.5$ previously analysed, although there are some quantitative differences. For example, note the rapid change of the critical helical mode structure n_c displayed in figure 10. The number of azimuthal modes to be considered in the stability analysis increases substantially in the narrow gap geometry. A case in point is circular Couette flow with radial heating (Ali & Weidman 1990) whereby the number of critical modes increases to $n_c = 52$ for $\eta = 0.959$ at Prandtl number $Pr = 4.35$. Tracking all these modes requires significantly more computation time.

Figure 11 shows the critical parameters R_{ic}, ω_c, α and c as functions of R_z and R_o for $\eta = 0.8$. The critical surface develops a cusp, but for higher positive values of R_z, outside the range plotted. The early stages of the cusp can be seen in figures 11(a), 11(c) and 11(d), where the curves display the same splitting in two different mechanisms as in the $\eta = 0.5$ case. We also notice that the shear-instability-dominated branch is very close to the solid-body rotation line (figure 11a). Additional numerical results in the region where the cusp is present will be given in § 5.1 when comparing with experimental results.

The $n = 0$ axisymmetric mode is stabilized by the axial sliding, giving axially travelling Taylor vortices. But now the dominance of the axisymmetric mode is restricted to a very narrow range of R_z values as shown in figure 10. From the numerical results, it could be asserted that the sliding has a global destabilizing effect on the basic flow. Another curious feature is the presence of a small window of the $n = -3$ critical mode between the regions $n = 2$ and 1. As it happens very close to the $R_z = 0$ axis, we consider it as a side effect of the mode competition and switching when the reflectional symmetry $z \to -z$ is broken.

5.1. *Comparison with previous results*

Some previous experimental studies have been reported on the stability of spiral Couette flow. In fact, in an excellent study by Ludwieg (1964), both theoretical and experimental, a stability analysis has been devoted to a specific zone in the parameter space, inside the cusp region. The experimental apparatus has a gap $\eta = 0.8$, with open ends, corresponding to our open flow case. The rotational speed of the external cylinder is held fixed at $R_o \approx 750$. Ludwieg's experimental device needed high external rotation speeds in order to avoid preturbulent stages induced by transients. The unique design of the experimental apparatus enforced a linear dependence between axial velocity and azimuthal rotation speed of the inner cylinder moving relative to an outer stationary cylinder (without axial velocity but rotating) for each orientation of the roller guides. As a result, the experimental paths in the parameter space (R_i, R_z)

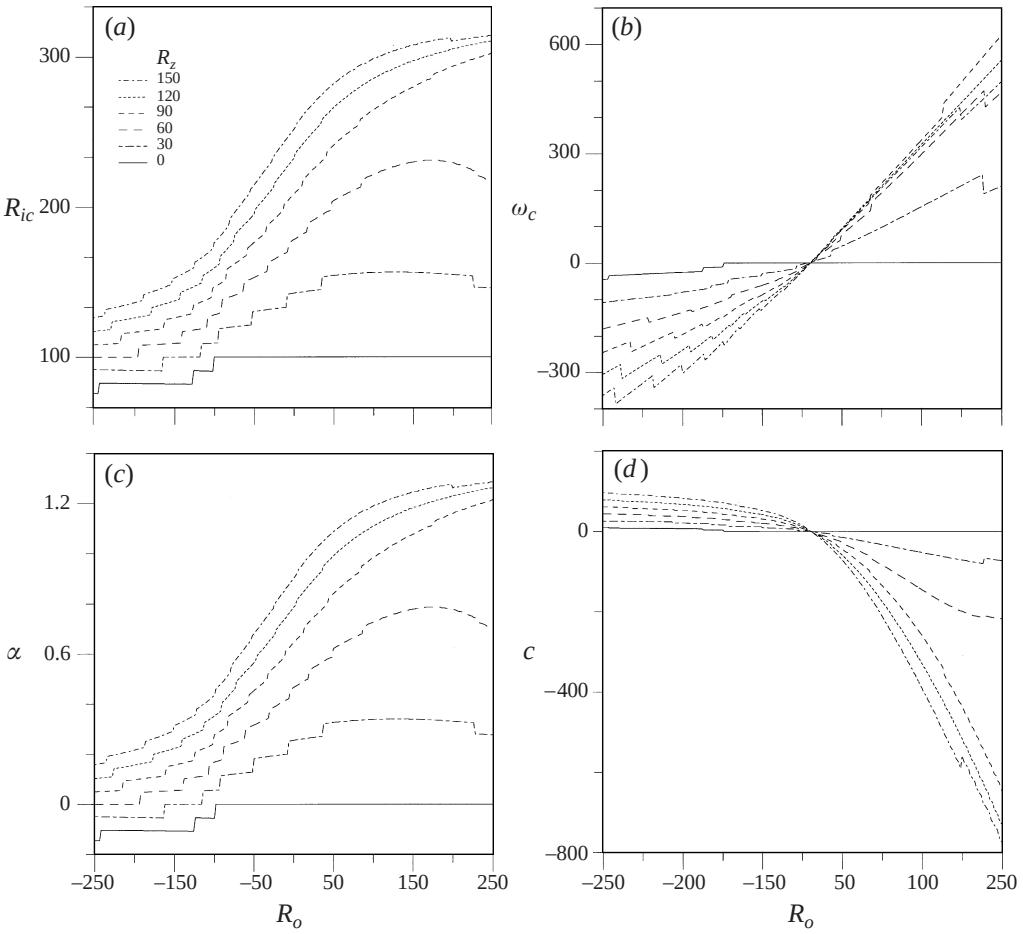

FIGURE 11. Critical parameters for $\eta = 0.8$. (*a*) Critical inner Reynolds number $R_{ic}(R_o)$; the solid straight line is the rigid rotation line $R_i = \eta R_o$. (*b*) Imaginary part of the critical eigenvalue ω_c. (*c*) Angle of the spiral pattern α in radians. (*d*) Axial pattern velocity c.

were straight lines, as can be seen in both figures 12(*b*) and 14. Ludwieg's experimental results (figure 12) are given in terms of two non-dimensional parameters c_ϕ and c_z which describe the motion of the fluid. These parameters are functions of the radial variable r,

$$c_\phi(r) = \frac{r}{v_B}\frac{\mathrm{d}v_B}{\mathrm{d}r}, \quad c_z(r) = \frac{r}{v_B}\frac{\mathrm{d}w_B}{\mathrm{d}r}, \tag{5.1}$$

where $r_i \leqslant r \leqslant r_o$. In some specific situations, these functions suffer only tiny variations in the prescribed range of values of r, mainly in the narrow gap case. As a consequence, Ludwieg (1964) considered mean values $\tilde{c}_\phi$ and $\tilde{c}_z$ of these functions as the control parameters; he took $r = (r_i + r_o)/2$, the arithmetic mean radius, for the r factor in front of the definitions of c_z and c_ϕ, but he did not specify which values of the azimuthal and axial velocities and their derivatives were used. Hung *et al.* (1972) used the values of $\tilde{c}_\phi$, $\tilde{c}_z$ at the geometric mean radius $\bar{r} = \sqrt{r_i r_o}$ to compare with Ludwieg's results. Since the difference between the arithmetic and geometric means is about 0.6% for the $\eta = 0.8$ case, and moreover, the expressions for $\tilde{c}_\phi$ and $\tilde{c}_z$ are simpler using the Hung *et al.* prescription, we adopt it; a more detailed discussion

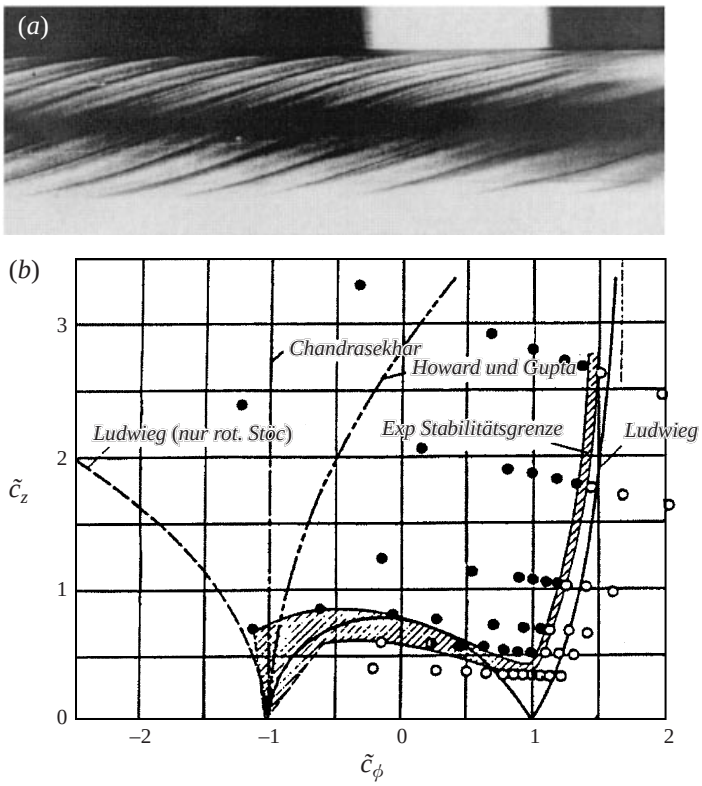

FIGURE 12. Ludwieg's experiments. (*a*) Picture of the spirals, from Wedemeyer (1967). (*b*) Experimental results, from Ludwieg (1964); $\eta = 0.8$, $R_o = 750$.

about the parameters used by different authors is given in Appendix B. Thus, the dependence between $\tilde{c}_\phi$, $\tilde{c}_z$ and our variables R_i, R_o, R_z are given by the following equations (for $\eta = 0.8$):

$$\tilde{c}_\phi = \frac{1+\eta}{1-\eta}\frac{R_o - R_i}{R_o + R_i}, \quad \tilde{c}_z = \frac{1+\eta}{1-\eta}\frac{R_z}{R_o + R_i}. \tag{5.2}$$

For the $\eta = 0.8$ case the narrow gap approximation is not clearly justified. In figure 13 we can see that the variation of the functions $c_z(r)$ and $c_\phi(r)$ is about 10% with respect to the mean values $\tilde{c}_z$, $\tilde{c}_\phi$. This can be a source of error in the experimental values given by Ludwieg (1964). It would be necessary to know the original experimental results in terms of the Reynolds numbers in order to work with the *true* control parameters R_z and R_i.

The experimental results of Ludwieg are summarized in figure 12(*b*). The shaded area is the error bandwidth experimentally obtained. These errors are very large in the fold region of the critical surface, and the reasons will be analysed shortly. Figure 12(*b*) also shows several stability criteria. Three of them, labelled *Ludwieg* (*nur rot. Stöc*), *Chandrasekhar* and *Howard und Gupta*, were obtained assuming axi-symmetric perturbations, and using physical considerations as in Rayleigh's criterion (labelled *Chandrasekhar* in figure 12*b*). All of them are in very poor agreement with the experimental data. Instead, Ludwieg's stability criterion, obtained by exactly solving the linearized Euler equations in the narrow gap limit, is reasonably close to the experimental data.

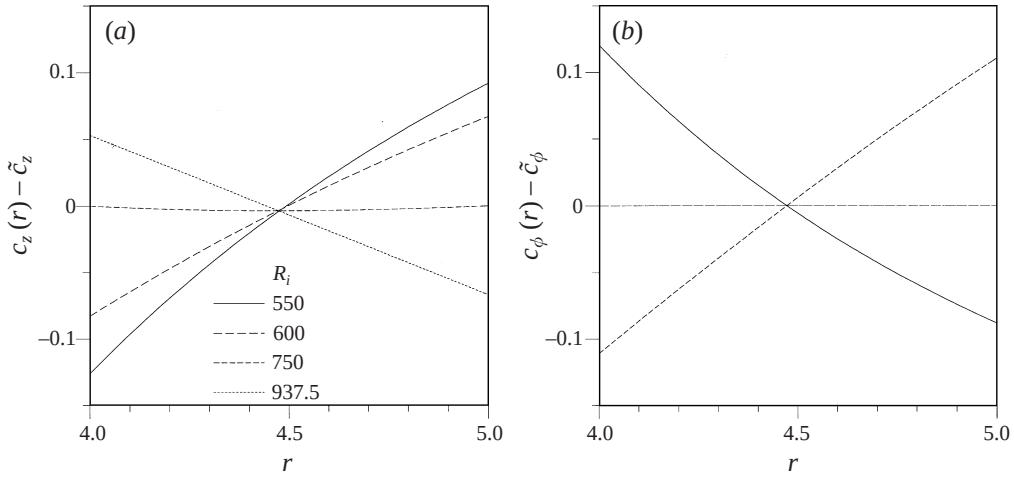

FIGURE 13. Variation of (*a*) $c_z(r)$ and (*b*) $c_\phi(r)$ for $\eta = 0.8$ in the gap, compared with the mean values $\tilde{c}_z$, $\tilde{c}_\phi$; as $c_z(r)$ is linear in R_z, we have plotted it only for the characteristic value $R_z = 100$.

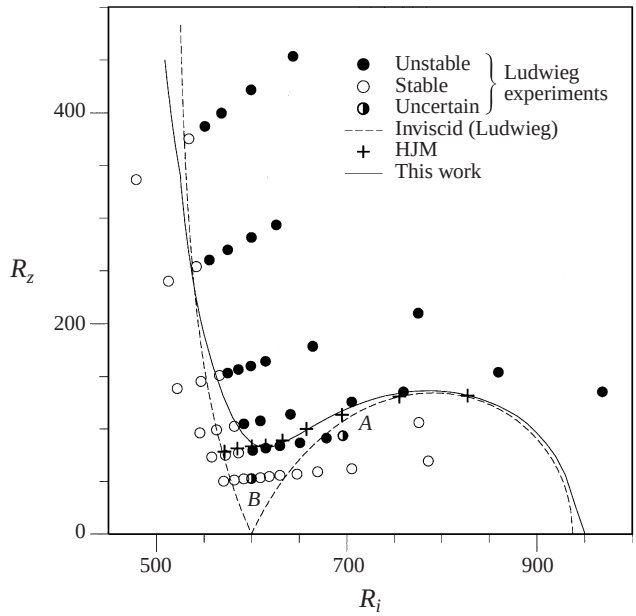

FIGURE 14. Comparison between the experimental and theoretical results of Ludwieg (1964), HJM and the present work. Parameters: $\eta = 0.8$, $R_o = 750$.

A linear stability analysis of the spiral Couette problem was reported by Hung *et al.* (1972, referred to from now on as HJM), where only particular regions in parameter space were considered. Their results are in good agreement with some of Ludwieg's results, although there were some unexplored zones that the present work has studied in detail. We have computed the critical curve for $R_o = 750$, which is single-valued considering $R_z(R_i)$, but it is well within the cusp region. The global results of the three analyses have been sketched in figure 14, which corresponds to the section $R_o = 750$ of the critical surface.

Our results fully coincide with the previous computations of HJM, except for two points on the left of the minimum of our critical curve in figure 14, where the results of HJM clearly diverge from the experimental results. It is apparent that the results of HJM are confined to the intermediate branch of the critical surface fold, where the changes in Rz_c are small. The other branches shows very high slopes of $Rz_c(R_i)$; furthermore, the change in the critical azimuthal wavenumber n is more than 15 units in this range. This is an indication of the difficulties HJM encountered outside the intermediate branch, which explains the discrepancy of their two computed points in the high-slope region of the stability curve.

The experimental results of Ludwieg show remarkable agreement with our numerical results. The best experimentally defined bifurcation points correspond to the vertical branch (where shear is the dominant instability mechanism), and on this curve the discrepancies with our results are less than 4%; we must mention that this is the first time the vertical branch has been computed numerically. The biggest discrepancy appears for high R_z, but for these parameter values, the splitting between the mean values $\tilde{c}_\phi$, $\tilde{c}_z$ and the functions $c_\phi(r)$, $c_z(r)$ has a maximum (see figure 13). In the region close to the minimum of the critical curve, the onset of instability is in very good agreement with the experiments, but some points on the right-hand side of the minimum clearly deviate from the numerical predictions. In order to understand why, we must look carefully at the experimental setting. In Ludwieg's experiments, a long rod (the inner cylinder) goes through the outer cylinder, with an axial movement and simultaneous rotation; the rod accelerates from rest to the final desired inner rotation and axial velocity. The experimental path follows the curves (containing the open and filled circles) in figure 14 from left to right. The experiment lasts until the rod has run through the outer cylinder, a short time interval in all cases. Coming back to figure 14, if we look at the two experimental series for low R_z (the two lowest curves), we see that to reach the point labelled A, when increasing the axial velocity of the rod, we cross the minimum of the instability curve, so a spiral flow appears before reaching A. Shortly thereafter, when the velocity continues growing, the basic flow again becomes stable, but now the flow is in the spiral regime, so we have different possibilities. If the spiral flow is also stable, the flow will not come back to the basic flow; if the bifurcation is subcritical, the spiral flow will persist within the region where the basic flow is stable (hysteresis effect). The spiral flow can also become unstable when we cross to the other side of the critical curve (supercritical bifurcation), but in this case too it will take a finite time for the spiral flow to decay into the basic flow. If we are close to the bifurcation point, which is the case of concern here, this time can be longer than the duration of the experiment. Making use of our linear stability analysis, we cannot decide which of these possibilities really occurs; weakly or fully nonlinear computations are required at this stage. These considerations help to explain why the experimental points close to A show a discrepancy with the current numerical computations. The experiment would have to be reconfigured using a path in parameter space not crossing the (multivalued) neutral stability curve, in order to be free of hysteresis and relaxation phenomena. Notice that the points A and B, marked with a black and white circle, where Ludwieg could not decide about their stability, are very close to the hysteresis region, strongly suggesting that the bifurcation could be subcritical in this region of parameter space. Ludwieg acknowledged the experimental uncertainties in this parameter region; figure 12(b) shows the estimated uncertainty as a dashed area.

Unfortunately, Ludwieg's experimental data do not include information about the azimuthal wavenumber n, or other raw order parameters such as the linear and

angular speed of the inner cylinder, and the observed angle of spiral inclination. Therefore our comparison is reduced to the analysis of stability boundaries in appropriate regions of (R_z, R_i)-space. Nevertheless, figure 12(*a*) shows a spiral mode with a large angle, corresponding to the shear-dominated branch; as figure 12(*b*) shows, the Ludwieg's experimental paths cross the critical surface through the mentioned branch. This feature is in complete agreement with the computed critical angle (figure 11*c*).

Finally we must mention the effectiveness of the inviscid criterion of Ludwieg, displayed as a dashed line in figure 14. The curve follows qualitatively the behaviour of the numerically computed viscous curve, and predicts a multivalued critical surface. The comparison between the inviscid criterion and our computations shows that viscosity stabilizes the flow, delaying the instability, except for high R_z, in the shear-dominated instability region, where the viscosity in fact destabilizes the basic solution, as has been observed in other shear flows.

6. Conclusions

In this work we have made a comprehensive analysis on the effect of axial sliding in the Taylor–Couette problem. We have developed specific and robust numerical methods to deal with the geometrical complexities of the neutral stability curves. We have tested our code by comparing with the results of Ali & Weidman (1993) for the capped endwall geometry. In the open geometry, detailed computations of the critical surface have been performed for two gap values. The wide gap $\eta = 0.5$ has been analysed in detail because the instability appears at lower Reynolds numbers than in the narrow gap case, and the change in the azimuthal wavenumber is also smaller. We have also considered the relatively narrow gap $\eta = 0.8$, because as far as we know, the only experimental data available on this problem correspond to this value. We have found that the sliding has a global destabilizing effect on the helical modes. By contrast, the $n = 0$ mode remains stabilized by the same effect, although the range of dominance of this behaviour is quite limited. The bifurcation is mainly to a spiral flow, but travelling Taylor vortices are also observed in small parameter ranges.

Remarkable differences can be pointed out between the co-rotation and counter-rotation zones. Counter-rotation configurations exhibit a regular behaviour in the critical regime. Nevertheless, we find a sudden dominance of non-consecutive azimuthal modes for low R_z values. This phenomenon is due to the breaking of the reflectional symmetry $z \to -z$, which leads to mode competition and switching between $\pm n$ modes.

The critical behaviour is radically different in the co-rotation zone. The critical surface $R_{ic} = f(R_z, R_o)$ exhibits zeroth-order discontinuities which can only be detected by making use of the specific numerical scheme for the computation of the neutral stability curves. The discontinuity is due to the presence of a sudden dominant island corresponding to a different azimuthal mode. This unusual phenomenon in hydrodynamical stability problems has been explained in terms of competition between two independent instability mechanisms: in the current problem the centrifugal instability, dominant in the counter-rotating regime and also for small axial sliding, competes with the shear instability induced by the axial motion. The latter mechanism becomes dominant near the solid-body rotation line, substantially lowering the onset of the instability. The discontinuity of the critical surface is associated with the competition between these mechanisms; the critical surface is folded into a cusp, and hysteresis behaviour becomes possible. The eigenfunctions corresponding to each mechanism are

clearly different: spirals with large angles correspond to shear-type eigenfunctions and show little variation of the azimuthal wavenumber n, while those corresponding to the centrifugal instability exhibit small spiral inclination angles, and large variations of n. We have found very good agreement with the computations of Hung *et al.* (1972), who obtained one of the branches in the fold region. The agreement with the experimental results of Ludwieg (1964) is also very good; in spite of the difficulties encountered with the parameters defined by Ludwieg, the agreement in the shear-dominated branch, computed for the first time, is better than 4%.

In order to precisely measure the bifurcation point in the region where hysteresis is present, new experiments should be performed, trying to avoid unwanted crossings of the critical surface, and designing a parameter path far from the tangencies exhibited by the lower experimental series of Ludwieg in figure 14. These experiments could also supply additional information about other critical parameters we have also computed.

The authors thanks Dr V. Iranzo for his help with the papers Ludwieg (1964), Kiessling (1963) and Wedemeyer (1967) (in German). This work was supported by the Dirección General de Investigación Científica y Técnica (DGICYT), under grant PB97-0685.

Appendix A. Matrix elements (Petrov–Galerkin scheme)

The spectral projections of the Petrov–Galerkin formalism are described explicitly by the following inner products:

$$G_{ij}^{11} = \int_{r_i}^{r_o} r\tilde{h}_i(r^2k^2 + n^2)h_j \mathrm{d}r; \quad G_{ij}^{12} = n\int_{r_i}^{r_o} r\tilde{h}_i \mathrm{D}_+ f_j \mathrm{d}r,$$

$$G_{ij}^{21} = n\int_{r_i}^{r_o} r(\mathrm{D}_+\tilde{f}_i)h_j \mathrm{d}r; \quad G_{ij}^{22} = \int_{r_i}^{r_o} r[k^2\tilde{f}_i + (\mathrm{D}_+\tilde{f}_i)\mathrm{D}_+]f_j \mathrm{d}r,$$

$$H_{ij}^{11} = \int_{r_i}^{r_o} \tilde{h}_i \left[r^2k^2\left(\mathrm{D}_+\mathrm{D} - \frac{n^2+1}{r^2} - k^2\right)r + rn^2\left(\mathrm{D}_+\mathrm{D} - \frac{n^2}{r^2} - k^2\right)\right] h_j \mathrm{d}r$$
$$-\mathrm{i}\int_{r_i}^{r_o} \tilde{h}_i\left(r^2k^2 + n^2\right)\left(\frac{n}{r}v_B + kw_B\right) r h_j \mathrm{d}r,$$

$$H_{ij}^{12} = n\int_{r_i}^{r_o} \tilde{h}_i \left[2k^2 f_j + r\left(\mathrm{D}_+\mathrm{D} - \frac{n^2}{r^2} - k^2\right)\mathrm{D}_+\right] f_j \mathrm{d}r$$
$$-\mathrm{i}\int_{r_i}^{r_o} \tilde{h}_i \left[k^2r^2\left(\frac{v_B}{r} + \partial_r v_B\right) + n\left(n\frac{v_B}{r} + kw_B\right)\mathrm{D}_+ + kn\left(\partial_r w_B\right)\right] f_j \mathrm{d}r,$$

$$H_{ij}^{21} = n\int_{r_i}^{r_o} \left[2k^2\tilde{f}_i + r\left(\mathrm{D}_+\tilde{f}_i\right)\left(\mathrm{D}_+\mathrm{D} - \frac{n^2}{r^2} - k^2\right)\right] h_j \mathrm{d}r,$$
$$+\mathrm{i}\int_{r_i}^{r_o} \left[2k^2 r v_B\tilde{f}_i - r\left(\mathrm{D}_+\tilde{f}_i\right)\left(n\frac{v_B}{r} + kw_B\right)\right] h_j \mathrm{d}r,$$

$$H_{ij}^{22} = \int_{r_i}^{r_o} \left[rk^2\tilde{f}_i\left(\mathrm{D}_+\mathrm{D} - \frac{n^2+1}{r^2} - k^2\right) + r\left(\mathrm{D}_+\tilde{f}_i\right)\left(\mathrm{D}_+\mathrm{D} - \frac{n^2}{r^2} - k^2\right)\mathrm{D}_+\right] f_j \mathrm{d}r,$$
$$-\mathrm{i}\int_{r_i}^{r_o} \left[\left(n\frac{v_B}{r} + kw_B\right)\left(k^2\tilde{f}_i + \left(\mathrm{D}_+\tilde{f}_i\right)\mathrm{D}_+\right) + k\left(\mathrm{D}_+\tilde{f}_i\right)\left(\partial_r w_B\right)\right] f_j \mathrm{d}r.$$

Appendix B. Parameters from different authors

The functions $c_\phi(r)$, $c_z(r)$ (5.1) introduced by Ludwieg (1964) are easily computed from the expressions (2.6):

$$c_\phi(r) = \frac{Ar^2 - B}{Ar^2 + B}, \quad c_z(r) = \frac{Cr}{Ar^2 + B}, \tag{B 1}$$

where the constants A, B, C are given by (2.7). Evaluating these expressions at the geometric mean radius $\bar{r} = \sqrt{r_i r_o}$, we get

$$\tilde{c}_\phi = \frac{1+\eta}{1-\eta}\frac{R_o - R_i}{R_o + R_i}, \quad \tilde{c}_z = -\frac{1+\eta}{\sqrt{\eta}\ln(1/\eta)}\frac{R_z}{R_o + R_i}. \tag{B 2}$$

By Taylor expanding near $\eta = 1$ we obtain

$$\frac{\sqrt{\eta}\ln(1/\eta)}{1-\eta} = 1 - \frac{(1-\eta)^2}{24} + \ldots, \tag{B 3}$$

therefore (5.2) are the narrow gap approximations of the expressions (B 2). In fact the expression for $\tilde{c}_\phi$ is exact, and the difference in $\tilde{c}_z$ is only 0.2% for $\eta = 0.8$, so we will use the expressions (5.2) from now on. The difference in sign has been introduced for better comparison with the experiments, because if we simultneously change the signs of R_z, n and ω_c the marginal stability curve does not change (see § 3 for a detailed account of the system symmetries).

The variables χ, $\tilde{\Omega}_2$ and R used by HJM are related to the present parameters by

$$R_i = R\left\{\frac{\eta}{1-\eta}\tilde{\Omega}_2 + \sin\chi\right\}, \quad R_o = \frac{R\tilde{\Omega}_2}{1-\eta}, \quad R_z = R\cos\chi. \tag{B 4}$$

Their dependence with the Ludwieg parameters $\tilde{c}_\phi$ and $\tilde{c}_z$ is

$$\tilde{\Omega}_2 = \frac{1 + a\tilde{c}_\phi}{\sqrt{(a+1)^2\tilde{c}_z^2 + (1-\tilde{c}_\phi)^2}}, \qquad \sin\chi = \frac{1-\tilde{c}_\phi}{\sqrt{(a+1)^2\tilde{c}_z^2 + (1-\tilde{c}_\phi)^2}}, \tag{B 5}$$

where $a = (1-\eta)/(1+\eta)$ and $R_o = 750$ is held fixed. From (B 4), (B 5) we can easily arrive at the same formulas (5.2), showing that HJM used the narrow-gap limiting values of $\tilde{c}_\phi$, $\tilde{c}_z$, or equivalently their values at the geometric mean radius $\bar{r} = \sqrt{r_i r_o}$.

REFERENCES

Ali, M. E. & Weidman, P. D. 1990 On the stability of circular Couette flow with radial heating. *J. Fluid Mech.* **220**, 53–84.

Ali, M. E. & Weidman, P. D. 1993 On the linear stability of cellular spiral Couette flow. *Phys. Fluids* A **5**, 1188–1200.

Canuto, C., Hussaini, M. Y., Quarteroni, A. & Zang, T. A. 1988 *Spectral Methods in Fluid Dynamics*. Springer.

Chida, K., Sakaguchi, S., Wagatsuma, M. & Kimura, T. 1982 High-speed coating of optical fibres with thermally curable silicone resin using a pressurized die. *Electronic Lett.* **18**, 713–715.

Chossat, P. & Iooss, G. 1994 *The Couette–Taylor Problem*. Springer.

Davis, S. H. & Rosenblat, S. 1977 On bifurcating periodic solutions at low frequency. *Stud. Appl. Maths* **57**, 59–76.

Edwards, W. S., Tagg, R. P., Dornblaser, B. C. & Swinney, H. L. 1991 Periodic traveling waves with nonperiodic pressure. *Eur. J. Mech.* B/*Fluids* **10**, 205–210.

Hart, J. E. 1971 Stability of the flow in a differentially heated inclined box. *J. Fluid Mech.* **47**, 547–576.

Hu, H. C. & Kelly, R. E. 1995 Effect of a time-periodic axial shear flow upon the onset of Taylor vortices. *Phys. Rev.* E **51**, 3242–3251.

Hung, W. L., Joseph, D. D. & Munson, B. R. 1972 Global stability of spiral flow. Part 2. *J. Fluid Mech.* **51**, 593–612 (referred to herein as HJM).

Isaacson, E. & Keller, H. B. 1966 *Analysis of Numerical Methods.* John Wiley & Sons.

Joseph, D. D. 1976 *Stability of Fluid Motions*, vols. I and II. Springer.

Ludwieg, H. 1964 Experimentelle Nachprufung des stabilitatstheorien fur reibungsfreie Stromungen mit schraubenlinienformigen stromlinien. *Z. Flugwiss* **12**, 304–309.

Kiessling, I. 1963 Uber das Taylorsche Stabilitatsproblem bei zusatzlicher axialer Durchstromung der Zylinder. *Duetsche Versuchsanstalt fur Luft-Unraumfahrt Bericht* 290.

Mackrodt, P. A. 1976 Stability of Hagen–Poiseuille flow with superimposed rigid rotation. *J. Fluid Mech.* **73**, 153–164.

Marques, F. & Lopez, J. M. 1997 Taylor–Couette flow with axial oscillations of the inner cylinder: Floquet analysis of the basic flow. *J. Fluid Mech.* **348**, 153–175.

Martin, J. E. & Meiburg, E. 1994 On the stability of the swirling jet shear layer. *Phys. Fluids* **6**, 424–426.

McFadden, G. B., Coriell, S. R., Murray, B. T., Glicksman, M. E. & Selleck, M. E. 1990 Effect of a crystal–melt interface on Taylor-vortex flow. *Phys. Fluids* A **2**, 700–705.

Meseguer, A., Marques, F. & Sanchez, J. 1996 Feigenbaum's universality in a four-dimensional fluid model. *Intl J. Bifurcation Chaos* **6**, 1587–1594.

Moser, R. D., Moin, P. & Leonard, A. 1983 A spectral numerical method for the Navier–Stokes equations with applications to Taylor–Couette flow. *J. Comput. Phys.* **52**, 524–544.

Mott, J. E. & Joseph, D. D. 1968 Stability of parallel flow between concentric cylinders. *Phys. Fluids* **11**, 2065–2073.

Ollis, D. F., Pelizzetti, E. & Serpone, N. 1991 Photocatalyzed destruction of water/contaminants. *Environ. Sci. Technol.* **25**, 1523–1529.

Sadeghi, V. M. & Higgins, B. G. 1991 Stability of sliding Couette–Poiseuille flow in an annulus subject to axisymmetric and asymmetric disturbances. *Phys. Fluids* A **3**, 2092–2104.

Sanchez, J., Crespo, D. & Marques, F. 1993 Spiral vortices between concentric cylinders. *Appl. Sci. Res.* **51**, 55–59.

Tadmor, Z. & Bird, R. B. 1974 Rheological analysis of stabilizing forces in wire-coating dies. *Polymer Engng Sci.* **14**, 124–136.

Temam, R. 1988 *Infinite Dimensional Dynamical Systems in Mechanics and Physics.* Springer.

Wedemeyer, E. 1967 Einfluss der Zahigkeit auf die Stabilitat der Stromung in einem schmalen Ringraum mit zusatzlichem, axialem Durchfluss. *AVA Bericht* **67**, A34.

Weisberg, A. Y., Smits, A. & Kevrekidis, I. 1997 Delaying transition in Taylor–Couette flow with axial motion of the inner cylinder. *J. Fluid Mech.* **348**, 141–151.